

SDSS J094604.90+183541.8: A GRAVITATIONALLY LENSED QUASAR AT $Z = 4.8$

IAN D. MCGREER,¹ PATRICK B. HALL,² XIAOHUI FAN,¹ FUYAN BIAN,¹ NAOHISA INADA,^{3,4} MASAMUNE OGURI,⁵ MICHAEL A. STRAUSS,⁶ DONALD P. SCHNEIDER,⁷ AND KARA FARNSWORTH¹

Draft version November 9, 2018

ABSTRACT

We report the discovery of a gravitationally lensed quasar identified serendipitously in the Sloan Digital Sky Survey (SDSS). The object, SDSS J094604.90+183541.8, was initially targeted for spectroscopy as a luminous red galaxy, but the SDSS spectrum has the features of both a $z = 0.388$ galaxy and a $z = 4.8$ quasar. We have obtained additional imaging that resolves the system into two quasar images separated by $3.06''$ and a bright galaxy that is strongly blended with one of the quasar images. We confirm spectroscopically that the two quasar images represent a single lensed source at $z = 4.8$ with a total magnification of 3.2, and we derive a model for the lensing galaxy. This is the highest redshift lensed quasar currently known. We examine the issues surrounding the selection of such an unusual object from existing data and briefly discuss implications for lensed quasar surveys.

Subject headings: gravitational lensing – quasars: individual (SDSS J094604.90+183541.8)

1. INTRODUCTION

Gravitationally lensed quasars offer the opportunity to study quasar host galaxies at a level of detail not otherwise accessible (Peng et al. 2006), sightlines to study the physical extent of intervening absorption structures (Ellison et al. 2004), and the means to constrain lens galaxy masses. Lensed quasar statistics are highly useful probes of cosmology, and time delays from individual lenses provide constraints on the Hubble constant (for a review see Kochanek 2006). Several approaches have been adopted to construct large samples of lensed quasars. One method is to obtain high-resolution images of a large number of sources to look for objects resolved into multiple images on small scales. This method has been applied at radio wavelengths by the CLASS survey, from which 22 lenses were found in a survey of $\sim 16,000$ radio sources (Myers et al. 2003; Browne et al. 2003). At optical wavelengths, the subarcsecond resolution required to identify most lenses has been achieved with HST snapshot surveys. Maoz et al. (1993) found five lenses in a sample of 502 quasars with $z > 1$; more recently, extensive HST follow-up of SDSS quasars at $z > 4$ yielded no lenses with $> 0.1''$ separation in a sample of 162 objects (Richards et al. 2004b, 2006). All of these searches can be considered more or less blind, in that little or no prior information was used to select lens candidates.

An alternative is to select likely candidates for lensed

quasars directly from imaging data. This is the approach taken by the SDSS Quasar Lens Search (SQLS: Oguri et al. 2006, 2008, Inada et al. 2008 and references therein, Kayo et al. 2009), which has identified 40 new gravitational lenses through follow-up of quasars within the SDSS. Candidates are selected either by the presence of a nearby object with similar colors as the quasar, or by the quasar having image being resolved, a hint that it may represent the blend of multiple images at small separations.

Only a handful of $z > 2.5$ quasars are currently known to be gravitationally lensed. Both blind and targeted surveys for lensed high redshift quasars are limited by the extreme rarity of the source population. That no lenses were found in the survey of Richards et al. — which included more than half of the $z > 4$ quasars known at the time — is unsurprising given lensing rates of $< 1\%$ found by surveys of quasars at lower redshifts (Inada et al. 2008; Browne et al. 2003); though the lensing probability increases with redshift (Turner et al. 1984) and magnification bias is expected to further enhance the observed lensing rate at high redshift in flux-limited surveys (for discussions of this effect on SDSS quasars, see Wyithe & Loeb 2002 and Comerford et al. 2002). Targeted surveys such as the SQLS further depend on the initial selection method employed to identify high-redshift quasar candidates. In the case of the SDSS, quasar targets at $z > 2.5$ are required to have a point-like morphology, introducing a strong bias against small-separation lensed systems.

We present the discovery of a $z = 4.8$ lensed quasar drawn from the SDSS. This is the highest redshift lensed quasar currently known, and only the third at $z > 4$, after BRI 0952-0115 at $z = 4.426$ ($1''$ separation, McMahan et al. 1992) and PSS 2322+1944 at $z = 4.12$ ($1.49''$ separation, Carilli et al. 2002; Riechers et al. 2008). SDSS J094604.90+183541.8 (hereafter J0946+1835) was initially targeted for spectroscopy as a luminous red galaxy and identified by strong quasar emission lines apparent in the SDSS spectrum.

This paper is organized as follows: in Section 2 we

¹ Steward Observatory, The University of Arizona, 933 North Cherry Avenue, Tucson, AZ 85721-0065

² Department of Physics and Astronomy, York University, 4700 Keele St., Toronto, ON, M3J 1P3, Canada

³ Cosmic Radiation Laboratory, RIKEN, 2-1 Hirosawa, Wako, Saitama 351-0198, Japan.

⁴ Research Center for the Early Universe, School of Science, University of Tokyo, Bunkyo-ku, Tokyo 113-0033, Japan.

⁵ National Astronomical Observatory of Japan, 2-21-1 Osawa, Mitaka, Tokyo 181-8588, Japan.

⁶ Princeton University Observatory, Peyton Hall, Princeton, NJ 08544, USA.

⁷ Department of Astronomy and Astrophysics, The Pennsylvania State University, 525 Davey Laboratory, University Park, PA 16802, USA.

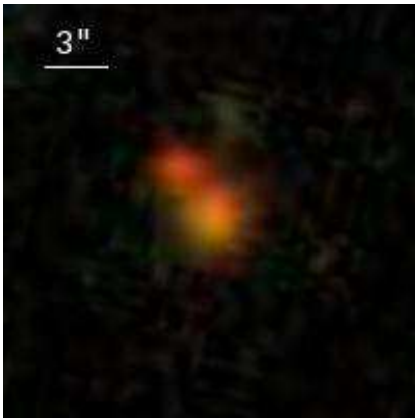


FIG. 1.— SDSS color image of J0946+1835. The image is centered on the photometric object targeted as a galaxy; the strong blending from additional, redder objects is apparent.

TABLE 1
SDSS PHOTOMETRY

Object	<i>g</i>	<i>r</i>	<i>i</i>	<i>z</i>
A	> 23.4	21.34 ± 0.14	19.52 ± 0.12	19.46 ± 0.11
B+G	20.90 ± 0.06	18.87 ± 0.01	17.98 ± 0.01	17.66 ± 0.02
<i>GALFIT</i> results:				
A'	> 23.4	21.42 ± 0.04	19.49 ± 0.02	19.53 ± 0.05
B'	> 23.4	20.46 ± 0.05	19.24 ± 0.04	19.30 ± 0.17
G'	20.89 ± 0.21	18.95 ± 0.06	18.30 ± 0.04	17.80 ± 0.08

NOTE. — The SDSS positions (J2000) are 09:46:04.90 +18:35:41.8 for A and 09:46:04.79 +18:35:39.7 for B+G. For object A the values are from PSF magnitudes, while for object B+G the values are model magnitudes; the SDSS photometry is given in asinh magnitudes (Lupton et al. 1999). Deblended photometry from GALFIT is given in the last three rows and described in §2.2; magnitudes are on the AB system.

show how the object was serendipitously identified from SDSS data and provide results from extensive photometric and spectroscopic follow-up that confirm the lensing hypothesis. We then provide results from modeling the lens galaxy (§ 3), briefly discuss the nature of the discovery of this object (§ 4), and conclude with prospects for future searches for high-redshift quasar lenses (§ 5). Unless otherwise noted, all magnitudes are on the AB system and corrected for Galactic reddening using the maps of Schlegel et al. (1998). We adopt a standard cosmology with parameters $H_0 = 70 \text{ km s}^{-1} \text{ Mpc}^{-1}$, $\Omega_m = 0.3$, $\Omega_\Lambda = 0.7$.

2. OBSERVATIONS AND DATA REDUCTION

J0946+1835 was targeted for spectroscopy by the SDSS as a Luminous Red Galaxy (LRG) according to the *gri* color selection technique outlined in Eisenstein et al. (2001). As we will discuss in § 4, this selection occurred because the foreground galaxy is significantly brighter than the background quasar images. In this section we present various observations of this system, beginning with the SDSS imaging and spectroscopy from which it was initially identified, followed by higher resolution and signal-to-noise ratio imaging, and finally spectroscopic observations of the multiple components comprising the system. All of these data provide strong evidence in support of the lensing hypothesis.

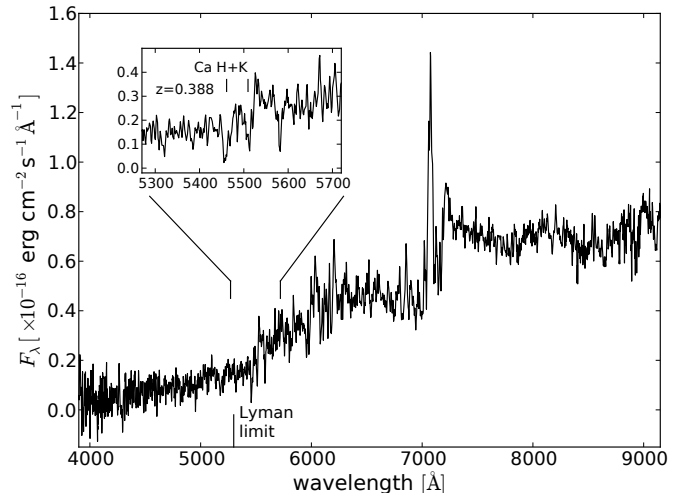


FIG. 2.— SDSS spectrum of J0946+1835, smoothed with a 5 pixel boxcar function. The Ly α and N V emission lines unambiguously show the signature of a $z = 4.8$ quasar. However, the level of flux blueward of Ly α (and in particular blueward of the Lyman limit) indicates excess light from another object; an expansion of the region around 5500Å shows that this object is a $z = 0.388$ galaxy.

2.1. SDSS Imaging & Spectroscopy

The SDSS is a photometric and spectroscopic survey covering nearly one-quarter of the sky (York et al. 2000). Images with the multi-CCD camera (Gunn et al. 1998) are obtained in five optical bands (*ugriz*) and reduced according to a photometric pipeline described in Lupton et al. (2001). Details of the photometric calibration procedure are given in Fukugita et al. (1996) and Smith et al. (2002), and the astrometric calibration is outlined in Pier et al. (2003). Photometric objects are selected for spectroscopy by various programs as detailed in Stoughton et al. (2002), including, among others, $\sim 10^5$ quasar targets (Richards et al. 2002a) and a similar number of Luminous Red Galaxy (LRG) targets (Eisenstein et al. 2001).

J0946+1835 was imaged during the course of the SDSS main survey on 2005 Mar 10 with seeing of $1.2''$, $1.2''$, and $1.5''$ in the *r*, *i*, and *z* bands, respectively. The SDSS photometric pipeline identified two objects in this field: a stellar object, and a much brighter galaxy located $\sim 2.4''$ to the SW. As we will show, this galaxy is actually an unresolved blend of a low-redshift galaxy and a high-redshift quasar. Although the galaxy is contaminated with quasar light, it was selected as an LRG spectroscopic target based on its *gri* colors. Details of the SDSS photometry from Data Release 7 (DR7, Abazajian et al. 2009) for the two objects are given in Table 1.

SDSS spectra are acquired with a multi-fiber spectrograph, with each fiber subtending a $3''$ diameter region on the sky. The spectra span 3800–9200Å at a resolution of ~ 1800 ; the wavelength and flux calibration of the spectra are described in Stoughton et al. (2002). A spectrum was obtained on 2006 Jan 24 with $1.3''$ seeing. The SDSS fiber was centered on the position derived for the B+G object. The spectrum clearly shows the emission line features of a $z = 4.8$ quasar (Figure 2). The spectrum also shows the Ca H+K absorption features of a $z = 0.388$ galaxy. The automated spectroscopic pipeline

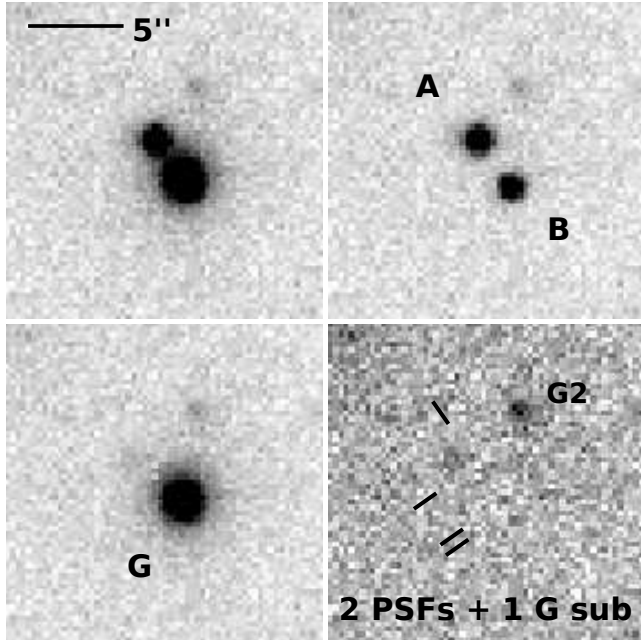


FIG. 3.— ARC SPIcam imaging of J0946+1835 with $0''.9$ seeing. North is up and east is left. The upper left panel shows a cutout image from the i band. Three components have been fit with GALFIT; the upper right panel shows the residual image after the model galaxy has been removed, while the lower left panel shows the residual image after the two model PSFs have been removed. The lower right panel shows the residual image with all model components subtracted, with lines whose intersections indicate the positions of each of the components. A faint galaxy ($i = 22.1$) remains visible to the NW, as well as a faint excess to the east.

spectro1d (Stoughton et al. 2002) classified the object as a quasar with low confidence (56%) and assigned redshift $z = 4.806$.

The complex nature of the spectrum became apparent from manual inspection during construction of the SDSS DR7 quasar catalog (Schneider et al. 2010). One author (DPS) identified 1083 spectra from DR6 and DR7 with quasar classifications but with questionable redshifts. From among those objects another author (PBH) identified six quasar/galaxy spectral blends whose SDSS images were consistent with a lensing hypothesis. Of those six, one had already been studied in the SQLS and found to be a quasar-galaxy pair, one was determined to be a quasar next to a $z = 0.0792$ galaxy, three are being followed up further, and the sixth is the object reported here.

2.2. ARC Imaging

J0946+1835 was observed with the SPIcam imager on the ARC 3.5m telescope at Apache Point Observatory on 2009 Nov 6. The 2048^2 backside-illuminated SITE CCD was binned by a factor of two along each axis during readout, resulting in a pixel scale of $0.28''$ over the $4.8'$ field of view. The seeing was $0.9''$ and conditions were photometric. Two dithered exposures of 240s each were obtained in the i -band and two dithered exposures of 300s each were obtained in the z -band. The images were reduced using standard IRAF⁸ routines called from

⁸ IRAF is distributed by the National Optical Astronomy Observatories, which are operated by the Association of Universities

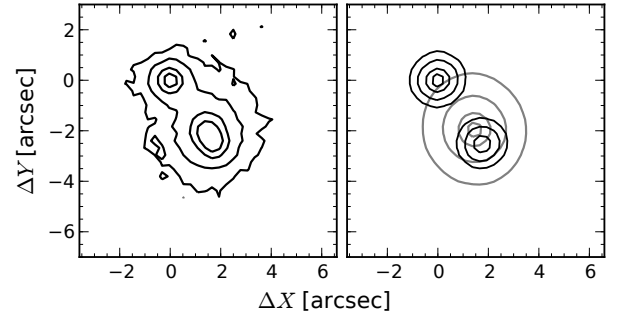


FIG. 4.— Contour plots of the ARC i -band imaging. Left panel: Total flux contours. Right panel: Contours of flux for the fitted components, including the two PSFs (black lines) and the model galaxy (gray lines). All contours are drawn at (19.6, 20.2, 21.4, 22.6) mag arcsec⁻², and positions are relative to A.

Pyraf⁹ scripts. After applying a bias correction, super-sky images for both filters were constructed by combining science images from other fields obtained just before the observations of J0946+1835; a total of seven i -band and 23 z -band images were used to construct the flats. Both astrometric registration and photometric calibration of the images were accomplished using bright SDSS stars within the field.

We derived positions and fluxes for the various components using the GALFIT code (Peng et al. 2002). For both the i and z images, approximate positions and fluxes obtained from examining the images with IRAF were used as initial conditions for the fitting. An empirical PSF was constructed from a set of 10 bright stars within the field. The fitting was then performed using two PSFs to represent the quasar images and a Sérsic model for the galaxy. Results of the fitting are shown in Figure 3 and Table 2. For the i -band image, the separation between the quasar images is $3.06''$ and the flux ratio is $f_B/f_A = 0.7$. Isophotal contours for the model components derived from the i -band imaging are displayed in Figure 4, showing the strong blending between B and G. Table 3 shows parameters for the Sérsic profile derived by GALFIT for the lens galaxy.

A faint galaxy is also seen $\sim 5''$ to the northwest (labeled G2 in Figure 3). This galaxy is not detected by the SDSS pipeline, but we were able to extract aperture photometry in the g , r , and i bands, and obtain a flux of $r = 22.0 \pm 0.1$ and colors $g - r = 1.3 \pm 0.3$ and $r - i = 0.3 \pm 0.2$. Photometry from the ARC imaging yields $i = 22.1 \pm 0.1$ and $i - z = 0.3 \pm 0.2$. These colors are inconsistent with an object at the redshift of the quasar, indicating that it is not an additional lensed image. However, this faint galaxy may be associated with the bright lensing galaxy. There also appears to be a flux excess (considerably fainter than galaxy G2) to the east of quasar image A in the SPIcam i band data.

2.3. UH88 Imaging

Additional imaging data of J0946+1835 were obtained on 2010 Jan 16 using the University of Hawaii 2.2m telescope (UH88) with the Tektronix 2048^2 CCD camera,

for Research in Astronomy, Inc., under cooperative agreement with the National Science Foundation.

⁹ Pyraf is a product of the Space Telescope Science Institute, which is operated by AURA for NASA.

TABLE 2
RELATIVE ASTROMETRY AND PHOTOMETRY

Component	ΔX (")	ΔY (")	V	UH88		ARC	
				R	I	i	z
A	0.000 ± 0.003	0.000 ± 0.003		21.05 ± 0.02	19.90 ± 0.01	19.76 ± 0.01	19.71 ± 0.02
B	1.756 ± 0.005	-2.503 ± 0.005		21.74 ± 0.07	20.00 ± 0.04	20.12 ± 0.03	19.82 ± 0.05
G	1.453 ± 0.005	-1.942 ± 0.008	19.37 ± 0.06	18.75 ± 0.02	18.06 ± 0.02	18.34 ± 0.01	17.96 ± 0.02

NOTE. — The reference position for component A is 09:46:04.90 +18:35:41.85 (J2000), with a systematic error in mapping to SDSS astrometry of $0''.06$ in each coordinate. All positions are derived from the ARC i -band imaging; positive X and Y represent west and north, respectively. Magnitudes are based on PSF models for A and B and Sérsic model for G, as calculated by GALFIT.

TABLE 3
PARAMETERS OF THE GALAXY PROFILE

	V	R	I	i	z
R_e (")	2.59 ± 0.26	1.56 ± 0.07	1.89 ± 0.11	1.24 ± 0.03	1.33 ± 0.05
e	0.29 ± 0.05	0.16 ± 0.02	0.13 ± 0.02	0.13 ± 0.01	0.13 ± 0.02
θ_e (°)	28.8 ± 6.5	14.2 ± 5.4	26.7 ± 7.0	16.6 ± 5.0	24.9 ± 8.6

NOTE. — All measurements taken from GALFIT results based on fitting a Sérsic profile with $n = 4$. The parameters are the effective radius (R_e), ellipticity ($e \equiv 1 - b/a$), and position angle of the ellipticity (θ_e , measured east of north).

TABLE 4
MULTI-EPOCH i -BAND PHOTOMETRY

Source	Epoch	A	B
SDSS	2005.19	19.49	19.24
ARC	2009.85	19.76	20.12
UH88 ^a	2010.04	19.82	19.92

NOTE. — Photometry for the two quasar images over three observational epochs.

^a UH88 i -band magnitudes are derived from the I -band imaging after computing a color difference from the observed SED of $I - i = 0.08$.

with a pixel scale of $0.22''$. Conditions were clear and photometric with 0.8 - $1.0''$ seeing. Images were obtained in the VRI bands; each band received four exposures of 120s each. Images were reduced using standard IRAF routines and photometric calibration was provided by the SA92 field. Magnitudes were derived on the Vega system and converted to AB using $V_{AB} = V_{Vega} + 0.00$, $R_{AB} = R_{Vega} + 0.20$, and $I_{AB} = I_{Vega} + 0.45$.

The UH88 images were also fit by three components using GALFIT using a similar process to that of the ARC imaging. Results of fitting the UH88 images are given in Tables 2 and 3. Overall, there is a high level of consistency between the positions derived by GALFIT in all of the imaging bands, and also between the UH88 and ARC imaging.

The galaxy G2 is detected in V , R , and I . As with the SPICAM i -band image, excess flux appears to the east of quasar image A in the UH88 I band image, indicating a real detection. There is a $\sim 1.4\sigma$ excess at this location in the V band; this object is also likely to be a low-redshift galaxy.

2.4. Imaging Summary

We have presented results from three epochs of imaging for this system, summarized in Table 4. There are some apparent differences when comparing the observations. We first note that the quoted photometric errors (Tables 1 and 2) are purely statistical errors from GAL-

FIT and do not reflect the uncertainties arising from the fitting itself and from the photometric calibration. The fitting uncertainties are particularly important for the SDSS imaging, which has the poorest resolution and the largest pixel size, hampering robust image decomposition. We have derived deblended photometry from the SDSS images by using GALFIT with some constraints to improve the fitting, namely, we fix the positions of the three components to the ARC-derived positions, and fix the galaxy fluxes to be within 0.1 mag of the ARC values¹⁰. The results of this fitting are shown in Table 1. We also experimented with unconstrained fitting of the SDSS images and had poor results. In particular, offsetting the initial positions by just a few pixels generally results in a fit with only two components, component B effectively being lost. This highlights the difficulty of fully characterizing a system such as this from SDSS imaging alone.

The colors of component B are slightly redder than those of component A in both the ARC and UH88 imaging, but not in the SDSS imaging. The ARC colors are $(i - z)_A = 0.05 \pm 0.02$ and $(i - z)_B = 0.30 \pm 0.06$; on the other hand, the SDSS colors are $i - z \approx 0$ for both components. The redder color of component B may be due to greater extinction from the lens galaxy; however, we argue against differential reddening of the two images in § 2.5. Some of the observed color differences between the two components are due to emission line differences of the quasar spectra, discussed in § 2.5. The remainder are likely due to the difficulty of decomposing the image properly, and are indicative of systematic errors in the photometry greater than the quoted statistical errors.

Component B is significantly brighter in the SDSS imaging than in either the ARC or UH88 imaging. While the fluxes measured for component A are roughly constant, component B appears to have faded by ~ 0.8 mag between the SDSS and ARC/UH88 epochs. While we have already concluded that systematic uncertainties in

¹⁰ For the g and r fluxes we used the V and R values from §2.3, and relaxed the constraint to ± 0.25 mag.

the photometry may be large ($\gtrsim 0.1$ mag), from experimentation with GALFIT we consistently find that B is brighter than A in the SDSS imaging. The relative fluxes of the two components may have changed due to intrinsic variability of the source quasar observed with a time delay between the two images, and/or differential microlensing of the two images. Component B is close to the center of the lens galaxy and its observed flux decrease is quite large; therefore, microlensing would seem to be the most likely explanation.

2.5. MMT Spectroscopy

Spectroscopic observations were obtained on 2009 Nov 11 with the Red Channel instrument on the MMT 6.5m. These observations were nearly contemporaneous with the ARC imaging, occurring only five days later. A single 1800s exposure was obtained with a $1.5''$ slit and the 270 mm^{-1} grating centered at 7500\AA . This provides a dispersion of $3.52 \text{ \AA pix}^{-1}$ at a spectral resolution of $R \sim 600$. The FWHM of unresolved emission lines from wavelength calibration exposures is 3.6 pix. The spatial pixel scale is $0.297 \text{ arcsec pix}^{-1}$. The seeing was $1''$ and thin clouds were passing overhead during the observation. The instrument was rotated to $\text{PA}=36.6^\circ$ in order to align the two components from the SDSS imaging in the slit.

Lamp exposures were obtained immediately subsequent to the science observation; however, a standard star observation was not obtained until the following night, using an identical spectrograph configuration but with somewhat better seeing. All images were reduced with standard IRAF routines, including a bias correction, flat fielding from a continuum lamp, wavelength calibration from HeNeAr lamps, and relative flux calibration from the standard star BD+284211 obtained on 2009 Nov 12. The science image was corrected for cosmic rays using the L.A. Cosmic routines (van Dokkum 2001).

The 2D spectra are strongly blended; in particular, components B and G are separated by only ~ 2 pixels ($0''.6$) perpendicular to the dispersion direction (rows in the MMT image, see Figure 5). We adopted a heuristic approach to extraction of the spectra with all three components deblended, similar to that of Pindor et al. (2004). First, the three spectra were treated as Gaussians fit independently to each row of the image, using a modified Levenberg-Marquardt algorithm from the SciPy library. We found that allowing all Gaussian components to vary and solving for all nine parameters led to clearly unacceptable results, even with reasonable initial conditions. We thus found it necessary to apply strong constraints to the Gaussian parameters in order to produce acceptable fits. We assumed that the standard star observation provides a model of the spectral trace on a 2D image, and then used this model to extract the blended science spectra, according to the following process:

1. A template trace for the 2D spectra was obtained from the high S/N observation of the standard star. This trace was used to derive the variation of the position and width of the spectrum along the image rows. The trace positions were fit with a 7th order polynomial, but they vary by only ~ 1 pixel across the full image.

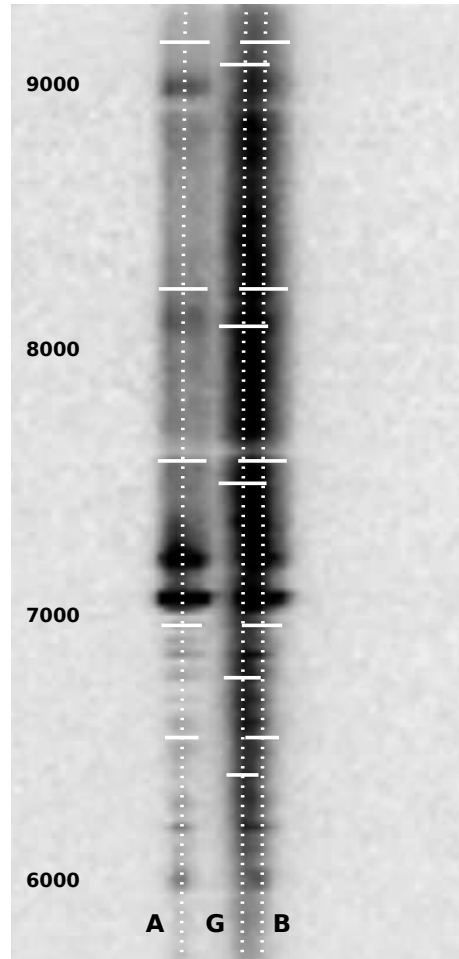


FIG. 5.— Two-dimensional spectra from MMT Red Channel observations. The spectral image has been binned by a factor of 8 along rows for display purposes (the spectral resolution is $R \sim 600$). Approximate wavelength positions along the dispersion axis (rows) are labeled. The traces for each component derived from Gaussian fitting are shown as dashed lines, while the FWHM of the fits are shown at various intervals with a horizontal line. The A spectrum is relatively unblended with the other two, while B and G are strongly blended.

2. Along each row of the science image, a Gaussian with three free parameters was fit to the leftmost columns of component A (those least affected by blending from G). This fit was compared to the template trace, and used to derive a translation of the template trace along the image columns to match the trace of A, as well as to derive a scale factor for the widths corresponding to the difference in seeing between science and standard star observations. This scale factor combined with the template widths provides an estimate of the widths of the point source components A and B.
3. The fit to A from step #2 was subtracted from the image. The same fit was then translated along columns to the position of B (as derived from the imaging) and subtracted again. The residual image is an approximation to the spectrum of G alone. Using the template trace again, fitting was performed on the residual image to derive the width of the galaxy spectrum along all rows.

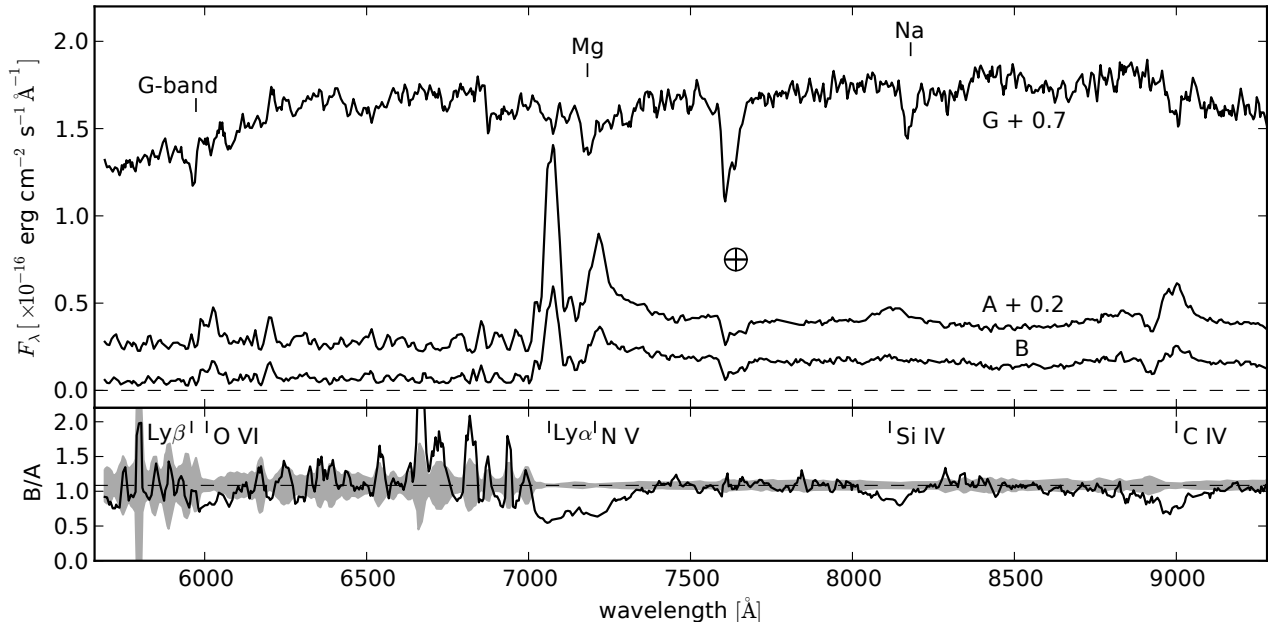


FIG. 6.— MMT Red Channel spectra of the components of J0946+1835. The upper panel shows the spectra extracted according to the procedure described in §2.5. The spectra have been smoothed to a dispersion of 10.6\AA , and scaled to the i -band fluxes derived from the image fitting of each component (Table 2). Constant offsets have been added to the spectra of A and G for display purposes. The striking similarity of the spectra for A and B, including the line profiles and absorption blueward of N V and C IV, provides strong evidence for the lensing hypothesis. Prominent elliptical galaxy absorption features are marked above the G spectrum, using the redshift for the galaxy derived from the Ca absorption seen in the SDSS spectrum (Figure 2). The A and B spectra have $S/N \sim 30 \text{ pix}^{-1}$ on the red side of Ly α and $S/N \sim 10 \text{ pix}^{-1}$ on the blue side. The lower panel shows the ratio of the B and A spectra after smoothing, with no scaling of the extracted spectra applied. The locations of the prominent quasar emission lines are indicated. The median ratio is ~ 1.1 in the continuum regions, but significantly lower around the emission lines. Uncertainties of $\pm 1\sigma$ in the ratio are shaded around the median value. Note that this is the observed flux ratio, and may differ from the actual ratio of the two components due to relative slit losses.

4. The previous steps provide estimates for the positions and widths of each spectral component based on expected positions derived from the imaging observations. However, the slit was likely not aligned perfectly on the center of each component. We then used the derived fits as initial conditions to a fit on the full 2D image. For this fit, the centers of the traces for each of the three components were offset by random amounts of up to ± 1 pixel along the columns. Fitting across the full image was then repeated 500 times with different initial offsets, allowing only the trace positions to vary. In other words, copies of the template trace derived from the standard star spectrum were varied in position until the best alignment with the three components was found. The positions from the best χ^2 among the repeated fits were then adopted as the best-fit positions for the 2D spectra.
5. Finally, with all positions and widths fixed, a fit was performed allowing only the amplitudes to vary along each row. The integrated Gaussians for the resulting amplitudes and widths were taken to represent the 1D spectra for each of the components.

Figure 6 shows the extracted spectra for the three components. The spectra have been scaled such that the synthetic i -band fluxes derived from the spectra match the i -band fluxes from the ARC imaging.

Several features of the spectra are worth noting. First, both the emission and absorption features of A and B show remarkable agreement, providing clear evidence that they represent lensed images of a single quasar at

a redshift $z = 4.8$. This cannot be due to incorrect extraction of the 2D spectra, as the Gaussians used to extract these two components are cleanly separated. While the line profiles of A and B are almost indistinguishable, the ratio of the two spectra shows that the emission line to continuum ratios are different. Component B is well within the effective radius of the galaxy, and differential microlensing of the continuum and broad line regions of B could explain this effect (e.g., Richards et al. 2004a). Alternatively, spectral variability could produce the discrepant line to continuum ratios, and cannot be ruled out by our single-epoch spectra. While the relative fluxes of the extracted spectra for the two components are uncertain due to possible differential slit losses, and the extraction was hampered by the strong blending of the B and G spectra, we are confident that the observed difference between the line to continuum ratios is not an artifact of our data. We have experimented with a large number of fitting parameters for extracting the 2D spectra, and in no viable fit does the B spectrum appear to be simply scaled from the A spectrum; in other words, the line ratios of the two components are always found to be significantly different from the continuum ratios.

In Section 2.4 we noted color differences between the two components of $\Delta(i - z) \approx 0.25$ mag, and considered whether differential reddening was affecting the observed colors. If one of the images, namely component B, was strongly affected by extinction from the lens galaxy, this would appear in the spectra as a difference in the shapes of the continua measured for the two components. Instead, the ratio of the continua measured for the two components is flat across $\sim 2000\text{\AA}$ of the observed wave-

TABLE 5
LENS MODELING RESULTS

$R_E(\prime)$	1.34 ± 0.03
e	0.41 ± 0.04
$\theta_e(^{\circ})$	-49.0 ± 1.4
$\Delta t(\text{days})$	142.7 ± 6.8
μ_{tot}	3.2

length range. However, some color differences should be introduced by the observed emission line differences. We derive synthetic i - and z -band magnitudes from the MMT spectra and find that the emission line differences contribute ~ 0.13 mag to the redder color of component B. This reduces the net color difference between the two components from the ARC imaging to ~ 0.12 mag, which is within the uncertainties.

The absorption features in the galaxy spectrum are exactly as expected for a luminous elliptical galaxy at $z = 0.388$, as derived from the Ca absorption features in the SDSS spectrum. This provides further confidence that the extraction was successful, as neither do the galaxy absorption features appear in the quasar spectra, nor do the quasar emission features appear in the galaxy spectrum.

We determine the quasar redshift to be $z = 4.8$ from the peak of the relatively narrow Ly α line, using the spectrum obtained for component A. The C IV line has significant absorption of its blue wing. A single Gaussian fit to the C IV line with the absorbed region masked results in a lower redshift of $z = 4.77$; however, the broad component of the C IV line is often blueshifted with respect to the systemic redshift (Richards et al. 2002b). We fit a power law continuum to the A spectrum and three Gaussians to the C IV line, one for a broad component, one for a narrow component, and one for the strong absorption. From this fit, the redshift of the narrow component is $z = 4.80$, in good agreement with the Ly α redshift, while the broad component is blueshifted by ~ 2000 km s $^{-1}$.

While the quasar spectra do show absorption features, particularly between Ly α and N V and blueward of C IV, the width of the C IV absorption is not strong enough to meet the criteria generally adopted for Broad Absorption Line (BAL) quasars (Weymann et al. 1991), though it has a non-zero Absorption Index ($AI = 140$ km s $^{-1}$) as defined by Hall et al. (2002) and may be a mini-BAL. This type of absorption appears in a minority of quasars and its identical shape in the spectra of both quasar images is strong evidence that they are lensed images of a single source as opposed to a binary quasar.

3. LENS MODELING

We model the system as a Singular Isothermal Ellipsoid (SIE) lens generating two images of the source quasar. We use the *lensmodel* code (Keeton 2001) to calculate the properties of both the lensing galaxy and the quasar. The positions and fluxes of each of the quasar images and the position of the lens galaxy obtained from the GALFIT fitting of the ARC i -band images are used to provide a total of 8 constraints. We solve for the position and flux of the source quasar, as well as the Einstein radius (R_E), ellipticity (e , defined as in Table 3), position angle (θ_e), and position of the lensing galaxy. As

the model has zero degrees of freedom, the *lensmodel* solution converges to $\chi^2 \sim 0$. The results derived from the ARC i -band imaging are given in Table 5, along with 1σ uncertainties ($\Delta\chi^2 = 1$). When fitting the lens model, positional uncertainties were increased by 50% and the flux uncertainties for all components were set to 5% in order to account for systematic uncertainties in deblending. The known redshift of the lensing galaxy ($z = 0.388$) enables us to estimate a time delay of 143 days.

There are some discrepancies between the galaxy light profile as measured from the imaging (Table 2) and the derived mass model (Table 5). If these discrepancies are real, one possibility is that they are due to shear (e.g., Keeton et al. 1998) from the nearby galaxies that were not included in the model.

4. DISCUSSION

Quasars in the SDSS have received extensive follow-up to identify lensed objects. The SQLS identifies candidate lensed quasars from the spectroscopically confirmed quasar sample using selection criteria outlined in Oguri et al. (2006). First, known quasars that are resolved in the imaging may represent two or more lensed images at small separations that are blended into single photometric objects within the SDSS database (morphological selection). Second, large separation lenses are selected by searching for nearby objects with similar colors as the quasar (color selection). Using these methods, Inada et al. (2009) recently identified five $z > 2.2$ lensed quasars in the SDSS. Two are $z > 3$ quasars targeted by the high redshift quasar selection criteria used by the SDSS (Richards et al. 2002a); for both objects, the two quasar images are separated by $> 1.5\prime$ and were successfully deblended by the photometric pipeline. J0946+1835 bears a strong resemblance to the $z = 3.6$ lensed quasar found by Johnston et al. (2003), which was also a galaxy targeted as an LRG by the SDSS and shown to be a high redshift lensed quasar by the presence of strong, broad emission lines in the SDSS spectrum.

It is instructive to consider whether J0946+1835 could have been selected as a lensed quasar candidate in the SQLS even if the lensing galaxy had not been targeted for spectroscopy by the SDSS. The SDSS registers J0946+1835 as two photometric objects, one a point-like object representing component A, and the other a resolved object representing a blend of B and G. The object representing component A is classified as stellar and its colors are relatively unaffected by the lensing galaxy, and thus it could have been considered as a quasar target by the SDSS. In fact, the object is well within the color selection criteria used by the SDSS to target $z > 4.5$ quasars (Richards et al. 2002a), with a dereddened PSF magnitude of $i = 19.52$ and colors $r - i = 1.82$ and $i - z = 0.06$. It was not considered as a quasar target because it has the photometric flag DEBLEND_NOPEAK set in multiple bands, indicating that no peak was found in the deblending. This means that the deblending, and thus the colors, are questionable, and the SDSS quasar target selection algorithm excludes such objects from its color selection.

Had component A not been flagged DEBLEND_NOPEAK, it would have been a primary quasar target in the SDSS. Once identified as a quasar, it would be further considered as a lens candidate

by the SQLS. Component A has a stellar classification in the SDSS and its PSF likelihood is high enough ($\text{star_L}(r)=0.06$ and $\text{star_L}(i)=0.07$) to fail to meet the morphological selection criteria of the SQLS (Oguri et al. 2006). In addition, the strong blending of the quasar and galaxy flux in the B+G object causes significant color differences between the two SDSS objects ($(r-i)_A - (r-i)_{B+G} = 0.93$), such that it would also fail to satisfy the color selection criteria. Thus, in the hypothetical (though generally expected) case that the stellar SDSS object was targeted as a quasar instead of the galaxy object being targeted as an LRG, this object would not have been identified as a lens candidate. It was fortuitous that the lensing galaxy was the object targeted for spectroscopy, as the blended quasar and galaxy features in the spectrum made the nature of the object evident. Furthermore, since the B+G object was spectroscopically identified as a quasar but clearly has the morphology of a galaxy, J0946+1835 will be included in the SQLS DR7 additional sample by modified morphological selection (see Section 5 of Inada et al. 2008).

Many of the difficulties encountered with selecting this object as a gravitational lens candidate arise from the bright lensing galaxy. The galaxy effectively hides the second quasar image, both in terms of detecting a second PSF image, as well as the blending of the galaxy and quasar colors. The galaxy also affected the well-separated quasar image by inducing additional photometric errors. High-redshift quasars have extremely red colors and are detected in only a few optical bands, and it is easy to imagine that similar lensed quasars may be hiding behind bright lensing galaxies. One way to find such objects is in the spectra of galaxy targets, as was the case here. This method has been used explicitly to find lensed background galaxies in the spectra of LRGs by the Sloan Lens ACS Survey (SLACS; Bolton et al. 2006).

5. CONCLUSIONS

We have identified the highest known redshift lensed quasar. J0946+1835 consists of a lens galaxy at $z = 0.388$ and a pair of quasar images produced from a source at $z = 4.8$. An object representing a blend of the lensing galaxy and one of the quasar images was targeted as a luminous red galaxy by the SDSS and classified as a quasar based on the spectrum. Subsequent observations show that the quasar images are separated by $3''$ and have a relatively low total magnification of 3.2. Comparison of photometry from three epochs indicates that there is variability of the two quasar images. Deblended spectra of the three components show that the two images represent a single quasar, and suggest that microlensing may affect the relative line equivalent widths, though spectroscopic observations spanning multiple epochs (preferably with higher spatial resolution) are needed to confirm this interpretation.

Continued photometric and spectroscopic monitoring of this object can be used to measure a time delay to compare with the value derived here, which constrains the Hubble constant (Refsdal 1964). Multiple spectroscopic epochs can also be used to look for variation of the quasar emission line equivalent widths consistent with a microlensing signature (e.g., Richards et al. 2004a), which

constrains the size of the broad line region. Lensing can also distort the host galaxy image away from the bright active nucleus such that it can be resolved (Peng et al. 2006). Probing the host galaxy of this object with HST imaging has the potential to allow the relationship between black hole mass and bulge mass to be examined for the most distant lensed quasar currently known.

This is the third high-redshift lensed quasar found in the spectrum of an object targeted by the SDSS as an LRG, joining the $z = 3.6$ lensed quasar reported by Johnston et al. (2003) and a $z = 2.2$ lens from the SQLS high-redshift sample (Inada et al. 2009). The SDSS-III¹¹ will target 1.5 million LRGs to a flux limit ~ 1.5 mag fainter than the SDSS-I/II; this fifteen-fold increase in the number of LRG spectra has the potential to result in a similar increase in discoveries of high-redshift quasars lensed by those galaxies and revealed by their spectra.

Another approach to identify quasars is by their variability (e.g., Schmidt et al. 2010; Kozłowski et al. 2010). Planned synoptic surveys such as PAN-STARRS (Kaiser et al. 2002) and LSST (Ivezic et al. 2008) will be able to identify high redshift quasar lenses through systematic searches for pairs of stellar objects at small separations that both vary (with a time delay), or by looking for resolved objects (galaxies) that vary (Kochanek et al. 2006). Oguri & Marshall (2010) predict that thousands of new lensed quasars will be discovered by upcoming time-domain surveys, including several hundred at $z > 4$ from the LSST alone.

6. ACKNOWLEDGEMENTS

We thank Jessica Evans and Chris Churchill for providing SPICAM flat fields. We also thank the anonymous referee for informative comments which improved the manuscript. IDM, XF and FB acknowledge support from a Packard Fellowship for Science and Engineering and NSF grant AST 08-06861. PBH acknowledges support from NSERC. N. I. acknowledges support from MEXT KAKENHI 21740151. MAS acknowledges support from NSF grant AST-0707266. DPS acknowledges support from NSF grant AST-0607634.

Use of the UH 2.2-m telescope for the observations is supported by NAOJ.

Funding for the SDSS and SDSS-II has been provided by the Alfred P. Sloan Foundation, the Participating Institutions, the National Science Foundation, the U.S. Department of Energy, the National Aeronautics and Space Administration, the Japanese Monbukagakusho, the Max Planck Society, and the Higher Education Funding Council for England. The SDSS Web Site is <http://www.sdss.org/>.

The SDSS is managed by the Astrophysical Research Consortium for the Participating Institutions. The Participating Institutions are the American Museum of Natural History, Astrophysical Institute Potsdam, University of Basel, University of Cambridge, Case Western Reserve University, University of Chicago, Drexel University, Fermilab, the Institute for Advanced Study, the Japan Participation Group, Johns Hopkins University, the Joint Institute for Nuclear Astrophysics, the Kavli Institute for Particle Astrophysics and Cosmology, the Korean Scientist Group, the Chinese Academy of Sci-

¹¹ <http://www.sdss3.org/>

ences (LAMOST), Los Alamos National Laboratory, the Max-Planck-Institute for Astronomy (MPIA), the Max-Planck-Institute for Astrophysics (MPA), New Mexico State University, Ohio State University, University of

Pittsburgh, University of Portsmouth, Princeton University, the United States Naval Observatory, and the University of Washington.

Facilities: ARC (SPICam), MMT (Red channel), UH:2.2m (Tek2k), Sloan

REFERENCES

- Abazajian, K. N., et al. 2009, *ApJS*, 182, 543
 Bolton, A. S., Burles, S., Koopmans, L. V. E., Treu, T., & Moustakas, L. A. 2006, *ApJ*, 638, 703
 Browne, I. W. A., et al. 2003, *MNRAS*, 341, 13
 Carilli, C. L., et al. 2002, *ApJ*, 575, 145
 Comerford, J. M., Haiman, Z., & Schaye, J. 2002, *ApJ*, 580, 63
 Eisenstein, D. J., et al. 2001, *AJ*, 122, 2267
 Ellison, S. L., Ibata, R., Pettini, M., Lewis, G. F., Aracil, B., Petitjean, P., & Srianand, R. 2004, *A&A*, 414, 79
 Fukugita, M., Ichikawa, T., Gunn, J. E., Doi, M., Shimasaku, K., & Schneider, D. P. 1996, *AJ*, 111, 1748
 Gunn, J. E., et al. 1998, *AJ*, 116, 3040
 Hall, P. B., et al. 2002, *ApJS*, 141, 267
 Inada, N., et al. 2008, *AJ*, 135, 496
 Inada, N., et al. 2009, *AJ*, 137, 4118
 Ivezić, Z., Tyson, J. A., Allsman, R., Andrew, J., Angel, R., & for the LSST Collaboration 2008, arXiv:0805.2366
 Johnston, D. E., et al. 2003, *AJ*, 126, 2281
 Kaiser, N., et al. 2002, *Proc. SPIE*, 4836, 154
 Kayo, I., Inada, N., Oguri, M., Morokuma, T., Hall, P. B., Kochanek, C. S., & Schneider, D. P. 2009, arXiv:0912.1462
 Keeton, C. R. 2001, arXiv:astro-ph/0102340
 Keeton, C. R., Kochanek, C. S., & Falco, E. E. 1998, *ApJ*, 509, 561
 Kochanek, C. S. 2006, *Gravitational Lensing: Strong, Weak and Micro*, Saas-Fee Advanced Courses, Volume 33. ISBN 978-3-540-30309-1. Springer-Verlag Berlin Heidelberg, 2006, p. 91, 91
 Kochanek, C. S., Mochejska, B., Morgan, N. D., & Stanek, K. Z. 2006, *ApJ*, 637, L73
 Kozłowski, S., et al. 2010, *ApJ*, 708, 927
 Lupton, R., Gunn, J. E., Ivezić, Z., Knapp, G. R., & Kent, S. 2001, *Astronomical Data Analysis Software and Systems X*, 238, 269
 Lupton, R. H., Gunn, J. E., & Szalay, A. S. 1999, *AJ*, 118, 1406
 Maoz, D., et al. 1993, *ApJ*, 409, 28
 McMahan, R., Irwin, M., & Hazard, C. 1992, *GEMINI Newsletter Royal Greenwich Observatory*, 36, 1
 Myers, S. T., et al. 2003, *MNRAS*, 341, 1
 Oguri, M., et al. 2008, *AJ*, 135, 520
 Oguri, M., et al. 2006, *AJ*, 132, 999
 Oguri, M., & Marshall, P. J. 2010, arXiv:1001.2037
 Peng, C. Y., Ho, L. C., Impey, C. D., & Rix, H.-W. 2002, *AJ*, 124, 266
 Peng, C. Y., Impey, C. D., Rix, H.-W., Kochanek, C. S., Keeton, C. R., Falco, E. E., Lehár, J., & McLeod, B. A. 2006, *ApJ*, 649, 616
 Pier, J. R., Munn, J. A., Hindsley, R. B., Hennessy, G. S., Kent, S. M., Lupton, R. H., & Ivezić, Z. 2003, *AJ*, 125, 1559
 Pindor, B., et al. 2004, *AJ*, 127, 1318
 Refsdal, S. 1964, *MNRAS*, 128, 307
 Richards, G. T., et al. 2002a, *AJ*, 123, 2945
 Richards, G. T., et al. 2006, *AJ*, 131, 49
 Richards, G. T., et al. 2004a, *ApJ*, 610, 679
 Richards, G. T., et al. 2004b, *AJ*, 127, 1305
 Richards, G. T., Vanden Berk, D. E., Reichard, T. A., Hall, P. B., Schneider, D. P., SubbaRao, M., Thakar, A. R., & York, D. G. 2002b, *AJ*, 124, 1
 Riechers, D. A., Walter, F., Brewer, B. J., Carilli, C. L., Lewis, G. F., Bertoldi, F., & Cox, P. 2008, *ApJ*, 686, 851
 Schlegel, D. J., Finkbeiner, D. P., & Davis, M. 1998, *ApJ*, 500, 525
 Schmidt, K. B., Marshall, P. J., Rix, H.-W., Jester, S., Hennawi, J. F., & Dobler, G. 2010, *ApJ*, 714, 1194
 Schneider, D. P., et al. 2010, *AJ*, 139, 2360
 Smith, J. A., et al. 2002, *AJ*, 123, 2121
 Stoughton, C., et al. 2002, *AJ*, 123, 485
 Turner, E. L., Ostriker, J. P., & Gott, J. R., III 1984, *ApJ*, 284, 1
 van Dokkum, P. G. 2001, *PASP*, 113, 1420
 Vestergaard, M., & Peterson, B. M. 2006, *ApJ*, 641, 689
 Weymann, R. J., Morris, S. L., Foltz, C. B., & Hewett, P. C. 1991, *ApJ*, 373, 23
 Wyithe, J. S. B., & Loeb, A. 2002, *ApJ*, 577, 57
 York, D. G., et al. 2000, *AJ*, 120, 1579